Effect of Ordered Intermediate Porosity on Ion Transport in Hierarchically Nanoporous Electrodes

Weon-Sik Chae,[†] Dara Van Gough,[‡,§] Sung-Kyoung Ham,[†] David B. Robinson,*[⊥] and Paul V. Braun[‡]

[†]Gangneung Center, Korea Basic Science Institute, Gangneung 210-702, South Korea

[‡]Department of Materials Science and Engineering, Frederick Seitz Materials Research Laboratory, and Beckman Institute, University of Illinois at Urbana−Champaign, Illinois 61801, United States

[§]Sandia National Laboratories, Albuquerque, New Mexico 87185, United States

[⊥]Sandia National Laboratories, Livermore, California 94550, United States

S *Supporting Information*
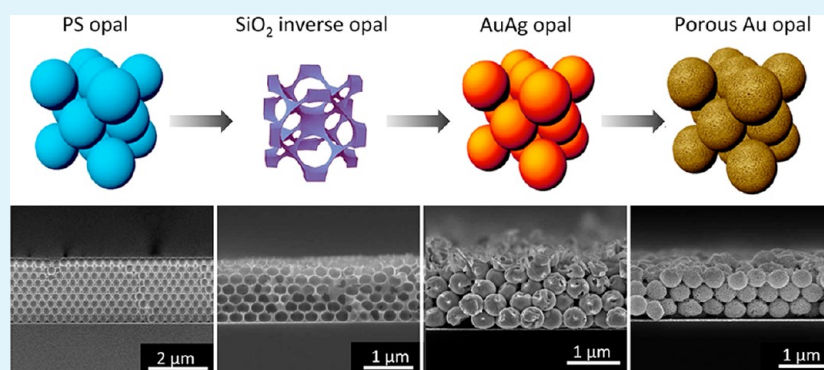
ABSTRACT: The high surface area of nanoporous electrodes makes them promising for use in electrochemical double-layer supercapacitors, desalination and pollution remediation, and drug delivery applications. When designed well and operating near their peak power, their charging rates are limited by ion transport through their long, narrow pores. This can be alleviated by creating pores of intermediate diameter that penetrate the electrode. We have fabricated electrodes featuring these by creating colloidal crystal-templated opals of nanoporous gold formed by dealloying. The resulting electrodes contain a bimodal pore-size distribution, with large pores on the order of several 100 nm and small pores on the order of 10 nm. Electrochemical impedance spectrometry shows that porous gold opals sacrifice some capacitance, but possess a lower internal resistance, when compared to a porous gold electrode with only the smaller-diameter pores. The architectural flexibility of this approach provides a greater ability to design a balance between power density and energy density.

KEYWORDS: *mesoporous, multimodal, ultracapacitor, admittance, frequency response*

Many important technologies such as electrical energy storage, catalysis, and chemical separations depend upon surface interactions. Nanostructured materials have extraordinarily high surface areas in a given volume, where every atom within the material is within a nanometer-scale distance from an interface. The disadvantage of these nanostructured materials is that transport of various species through the long, narrow pores can be slow.[1] In the case of capacitive energy storage, the charging time is proportional to L^2/r, where L is the length and r is the radius of the pore.[2,3] For fluid flow, the dependence on pore radius can be stronger. In electrochemical capacitors, the finite ion size relative to the pore radius and other nanoscale effects can restrict transport in the narrowest pores. In small pores, adsorption of ions to the surface can cause significant depletion of ions from the liquid, increasing its resistivity.[4] Transport limitations can be alleviated if a network of wider pores penetrates a material with narrow pores.[5−7] For electrical energy storage, finely interpenetrated electrodes are desirable.[8]

A simple implementation of a pore hierarchy could be a packed powder of nanoporous particles.[9] An optimal design would most likely involve an ordered arrangement of identical subunits. Such a design would also be easy to model, allowing experimental verification of design principles, and it may provide a useful step toward synthesis of interpenetrated, hierarchical electrode structures widely recognized as key to orders-of-magnitude improvements in power density in electrical energy storage devices.[8] We present a new path to ordered hierarchically nanoporous conductors to help advance this effort, and investigate the effect of that order on charging rates of electrochemical capacitor electrodes made from them.

Specifically, we create hierarchically porous opals of mesoporous gold. Porous gold containing a network of 10–20 nm pores can be prepared by selectively dealloying the less noble silver from silver–gold alloys.[10-14] This technique has primarily been used to form film or foil sample geometries, but some architectures with multiple designed length scales have been prepared.[15] Gold serves as an ideal model material because it is chemically stable, it can be surface modified, and significant effort was previously expended to understand its behavior.[16-19] Synthetic opals, close-packed assemblies of monodisperse colloidal spheres, are used as templates. These colloidal crystals were prepared by sedimentation and were subsequently infiltrated with a second material to create an inverse structure. We utilize this inversion process to template the electrodeposition of a silver–gold alloy. Upon removal of the less noble silver and template, a mesoporous gold opal is obtained. Comparison of the capacitive charging rates of these electrodes shows that intermediate levels of porosity involve some loss of energy density, but permit high power densities to be obtained at different frequencies from those possible for nonhierarchical structures.

EXPERIMENTAL SECTION

Preparation of Poly(Styrene) Colloidal Assemblies. A sedimentation method was utilized for the fabrication of poly(styrene) (PS) colloidal assemblies.[20,21] The substrate was prepared by the electron beam (E-beam) evaporation of a gold film (30 nm thickness on top of ~2 nm chromium adhesion layer) on a silicon wafer. The gold-coated wafer was treated with (3-mercaptopropyl)-trimethoxysilane (MPTMS, Aldrich, 95%) by soaking in MPTMS ethanol solution (0.2%, v/v) overnight. A transparent Tygon tube (R-3603, AAC00022, 8 mm inner diameter) was adhered to a substrate using an epoxy glue, Figure 1a. In a typical sedimentation, 0.1 mL colloidal suspension of 0.1 vol % poly(styrene) latex (D = 466 nm, IDC Inc.) with sulfate and carboxylate surface functionality, dispersed in a mixed solvent (20 vol % ethanol in water), was added to the tube. The solvent was allowed to slowly evaporate at ambient temperature overnight, and then the tube was removed with a blade. The resulting sediment showed opalescence, which indicated an ordered assembly of PS spheres, Figure 1b.

Preparation of silica Inverse Structures Using the Poly-(Styrene) Colloidal Assemblies As Templates. Silica inverse structures were synthesized from the sedimentation-induced ordered PS assemblies grown on the MPTMS-treated gold-coated Si wafers by infiltrating with a silica precursor mixture, which consisted of 1.20 mL of tetraethyl orthosilicate (Sigma-Aldrich), 3.00 mL of ethanol, 0.26 mL of deionized water, and 0.24 mL of hydrochloric acid (0.1 M, Showa chemical). Samples were placed in a 55 mm dish and submerged in this solution for 1 h, allowing partial evaporation of the solvent. During this step, the interstitial space between PS spheres in the opals was infiltrated with the precursor solution through capillary action. After the silica precursor-infiltrated PS assemblies were removed from the precursor solution, they were placed into a mixed solvent (80 vol % ethanol in water) for 8–10 s, a step that prevents formation of silica above the opal surface. The resulting composite PS opal was dried at ambient temperature overnight. Finally the template PS spheres were removed by soaking in toluene, which resulted in silica inverse structures. In this step, the MPTMS layer enhanced silica inverse opal adhesion to the gold substrate. However, application of strong fluid flow or capillary forces can still damage these structures.

Electrochemical Deposition of Porous Gold Materials. Electrodeposition into the silica inverse structures was performed in a three-electrode cell with a Pt counter electrode and an Ag/AgCl reference electrode in a fritted glass tube. The gold film under the silica inverse opal template served as the working electrode. The templates were carefully immersed into a plating solution, which consisted of an aqueous solution of 0.02 M KAu(CN)$_2$, 0.05 M KAg(CN)$_2$, and 0.25
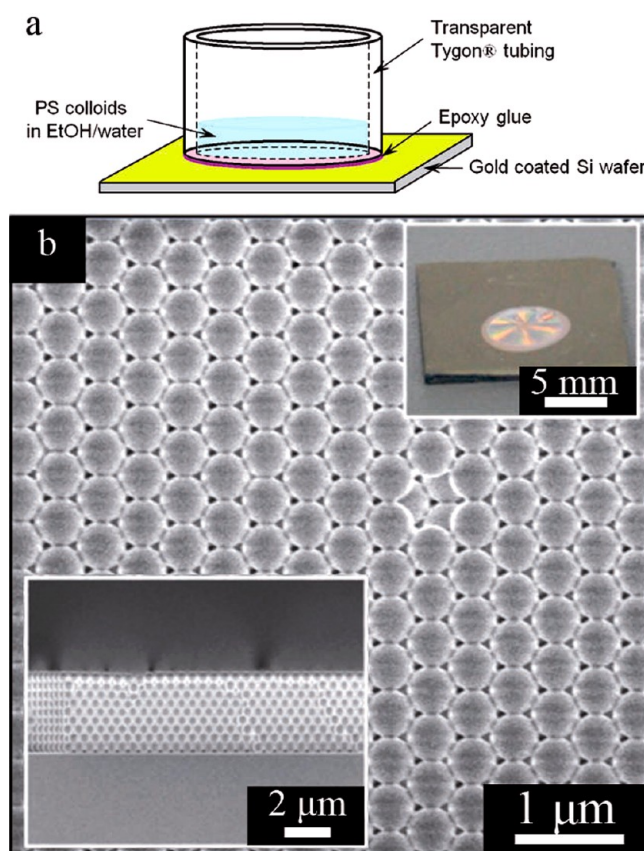

Figure 1. (a) Schematic showing the colloid sedimentation cell. A Tygon tube was bonded to a gold coated substrate; the colloid is placed within the tube and allowed to dry. (b) SEM image of a poly(styrene) opal (lower left inset: cross-section SEM image of the opal; upper right inset: picture of the sample showing opalescence).

M Na$_2$CO$_3$. Deposition was performed at −0.95 V (vs Ag/AgCl) in a pulsed manner (5 s at −0.95 V and 5 s at 0 V). The silica was then removed from the resultant composite structure by etching using a 10% by weight HF solution (caution: very toxic) for 15 min. The sample was subsequently etched with a concentrated nitric acid solution (caution: strongly corrosive) for 20 min to dissolve the Ag metal. The resultant structures were bimodally porous gold (p-Au) materials (Figure 2). A continuous p-Au reference film was electrochemically deposited on the substrate without a colloidal assembly template using t this plating solution.

For the preparation of the solid gold opal (without pores in spheres) for a comparative study, electrodeposition into the silica inverse opal was conducted in a plating solution consisted of 0.02 M KAu(CN)$_2$ and 0.25 M Na$_2$CO$_3$ at −0.95 V (vs Ag/AgCl) in the same pulsed manner as the bimodal p-Au for 220 cycles. As above, the silica template was removed by etching in 10% by weight HF.

Characterization. Imaging and elemental analysis of the fabricated materials were performed using a field emission scanning electron microscope (FE-SEM, SU-70, Hitachi) equipped with an energy dispersive X-ray spectrometer (EDX). Cyclic voltammetry (CV) and electrochemical impedance spectroscopy (EIS) measurements were performed using a computer controlled potentiostat (VMP3, BioLogic Scientific Instruments) in aqueous electrolyte solutions (solution details are provided in figure captions) versus an Ag/AgCl reference in 3 M KCl.

RESULTS AND DISCUSSION

A (PS) colloidal assembly deposited onto an evaporated gold substrate shows opalescence and a highly ordered array of the component PS spheres, Figure 1b. This PS opal is used as a
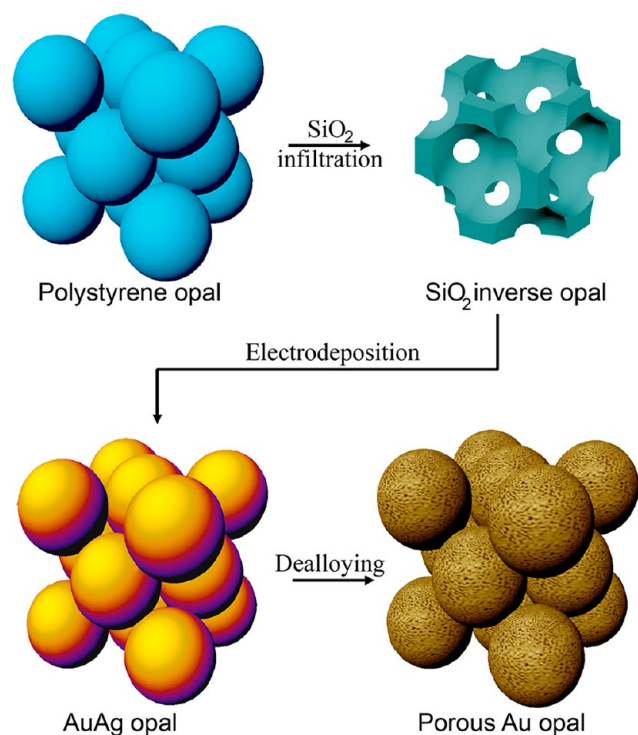
3974

dx.doi.org/10.1021/am300798j | ACS Appl. Mater. Interfaces 2012, 4, 3973–3979

Figure 2. Scheme of preparation of bimodal porous gold materials via a double templating route. A poly(styrene) colloidal crystal deposited onto a Au film was subsequently infilled with SiO$_2$. After removal of the poly(styrene) template, an Au/Ag alloy was electrodeposited into the void space of the silica inverse template. Finally, a bimodally porous Au structure was formed by removal of the SiO$_2$ template and Ag.

template for a silica inverse opal by applying a series of processes: filling with the silica precursor, sol−gel condensation, and PS sphere removal, shown schematically in Figure 2. To prepare bimodally porous gold (p-Au) materials, we electrodeposited a gold−silver (AuAg) alloy into an inverse opal template (Figure 3a), then used a dealloying process, in which the less noble component (Ag) of the solid solution is etched away. Additionally, an opal consisting of nonporous gold spheres (Figure 3e, f) was fabricated by electrodeposition of gold into an inverse opal template. A p-Au continuous film can be easily fabricated on an evaporated gold substrate by the same elctroplating and dealloying process (Figure 3b). This film was about 2.5 μm thick. Plating and dealloying can be performed using silica inverse opals as templates. After alloy deposition, removal of the silica template, and silver dealloying, an assembly of p-Au balls is obtained, which is the counterpart of the original PS opal template (Figure 3c, d, and g). The porous Au opal has unique bimodal porosity with small mesopores of ~10 nm and large pores formed by the interstitial space of 40−100 nm. Volume loss from the spheres during dealloying contributes to greater spacing between them. The overall film thickness is about 2 um (6 layers) for the procedure reported here, as measured in an SEM cross section (Figure 3g) but varying the volume of PS suspension added can vary the film thickness. The spheres are interconnected, and not easily dispersed, but become more disordered during sectioning, as in Figure 3g. Energy-dispersive X-ray spectroscopy reveals that the p-Au materials consist of predominantly of gold with trace amounts of silver.

Using the fabricated porous Au electrode materials, we determined electrochemical activity by collecting cyclic voltammograms in 1 M H$_2$SO$_4$. When scanning to positive potentials, the characteristic oxidation peak for gold is observed at ~1.2 V. On reversing the scan, a characteristic peak for gold oxide reduction is observed at ~0.9 V.[22] The area under this peak is proportional to the surface area. Surface areas are reported in Table 1, with the assumption that gold oxide charges to 390 μC/cm^2.[23] It is highest for the continuous porous film, because that film is slightly thicker, and contains the most dealloyed gold within that thickness.

The position of the oxide reduction peak varies between 0.7 and 0.9 V (Figures 4 and 5) shifting more negative at faster scan rates. The effect is greatest for the bulk film, less for the porous opal, and lowest for the solid opal. We attribute the shift to the IR voltage drop outside of and within the pores due to the higher currents being passed. This causes the gold oxide to be reduced later in the scan, resulting in a negative peak shift.

To explore the charging rates in more detail, cyclic voltammograms were performed in sodium trifluoroacetate. The sodium and trifluoroacetate ions have similar mobilities, and any specific adsorption of these ions is believed to be relatively weak.[24] The lack of peaks in the voltammogram in Figure 6 suggests that the electrode behaves like a linear resistor-capacitor network in the range between −0.1 and 0.1 V with respect to Ag/AgCl. Given this result, electrochemical impedance spectroscopy (EIS) in this range provides a more direct measure of transport within the porous gold electrodes. There are gradual slopes in the voltammograms of the dealloyed samples that we attribute to a slow redox current from residual silver. As will be seen, this does not interfere with EIS measurements on the time and current scales of interest.

EIS measurements were performed by applying a sinusoidal voltage with a zero-to-peak amplitude of 100 mV, with no offset. Two quantities of interest that can be derived from the EIS data are the complex capacitance ($1/i\omega Z$), the real component of which is proportional to the energy stored at a given frequency, and the admittance ($1/Z$), the imaginary component of which is proportional to the power delivered at a given frequency. The real admittance is proportional to the power dissipated at that frequency.[26]

Figure 7 shows the real part of the complex capacitance. The porous film shows the highest values at low frequency, but at higher frequencies, resistance prevents full charging of the capacitance. In this range, the porous opal stores more energy. There is also a region at higher frequency where the solid opal stores more energy, even though its low-frequency value is much lower.

The behavior in this region can be understood in greater detail by considering the admittance. Figure 8 shows the admittance as a function of frequency for each electrode type. The admittance of a pure capacitor is $i\omega C$, which is observed as an imaginary component with a slope such that an order of magnitude increase in admittance results from an order of magnitude increase in measurement frequency. An imaginary component with this slope indicates that complete charging and discharging of the electrochemical double layer occurs within the period of the applied waveform. When capacitance is dominant, the real component is smaller, and more steeply sloped. In Figure 8, these trends are observed at low frequency for each electrode type. The capacitance of the continuous porous film is higher than that of the porous opal, which is in turn higher than the solid opal. This is consistent with the
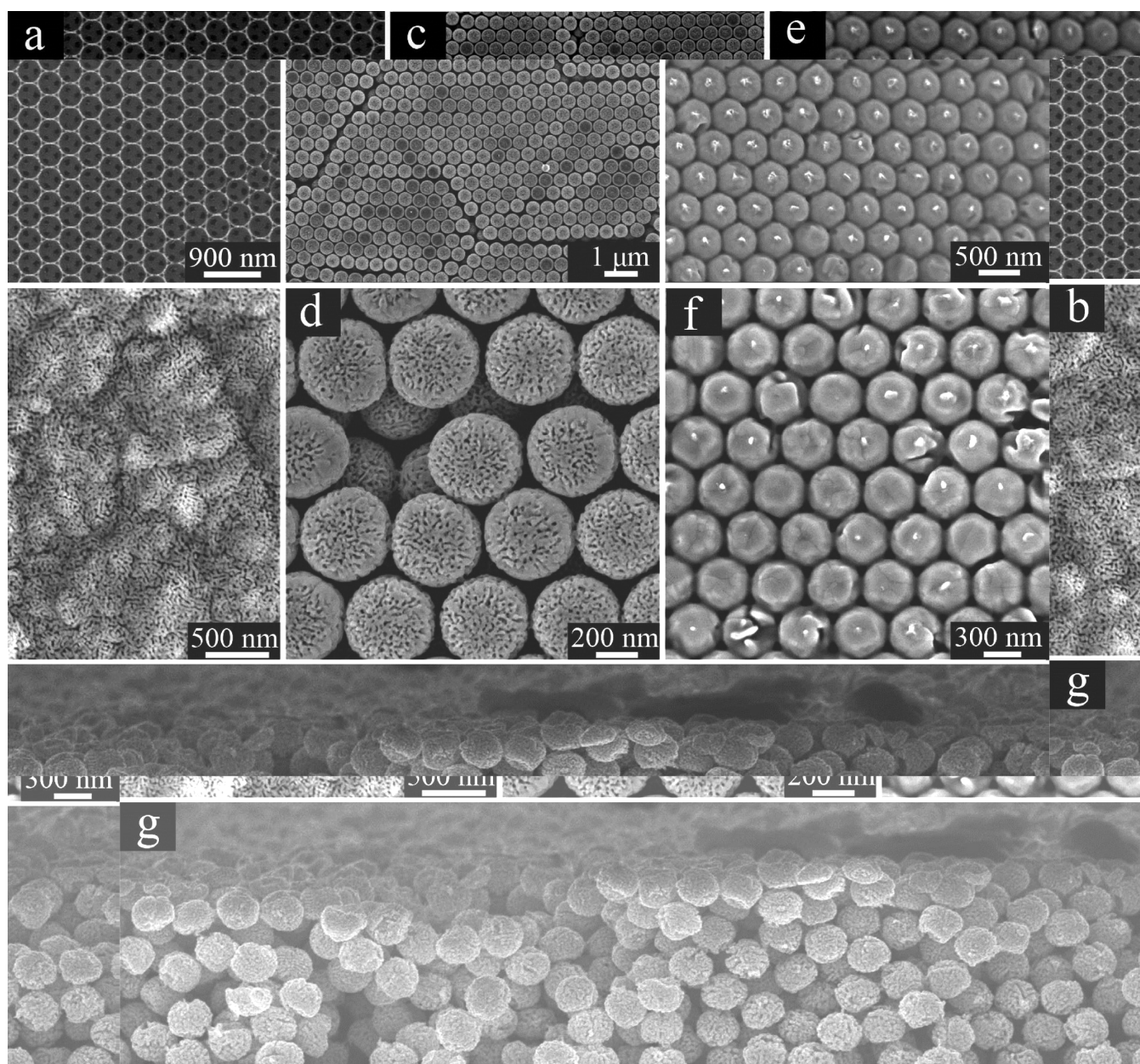
Figure 3. Scanning electron microscope images showing: (a) a silica inverse opal template; (b) a porous gold film obtained by electrodeposition without the use of an opal template; (c, d) low- and high-magnification SEM images, respectively, of a porous gold opal; (e, f) low and high-magnification SEM images, respectively, of a gold opal; (g) cross-section of porous Au opal.

Table 1. Surface Area As Determined by the Gold Oxidation Peak Area[23] and De Levie Model Parameters[24] for the Three Types of Electrode in 30 mM Sodium Trifluoroacetate[a]

sample	surface area (cm²)	external resistance, R_x (Ω)	internal resistance, R_i (Ω)	capacitance, C (μF)	branch external resistance, $R_{x,b}$ (Ω)	branch internal resistance, $R_{i,b}$ (Ω)	branch capacitance, C_b (μF)
solid opal	4.1	140	450	20	--	--	--
porous film	43.6	130	150	20	200	500	210
porous opal	20.3	130	1200	20	300	200	100

[a]No branch was used to fit the solid opal.

results from the surface oxidation and reduction experiment, because we expect both to be proportional to surface area. At very low frequencies (and rather small signals), a deviation is observed, mostly in the real component, and most prominently for the alloy electrodes. We attribute this to a slow redox

current from residual silver, as also seen in the voltammogram (Figure 6), but claim that the residual silver does not affect the behavior at higher currents and faster time scales. This can also be seen in the impedance (Nyquist) plots shown in Figure S1 of the Supporting Information. A pure capacitance can be
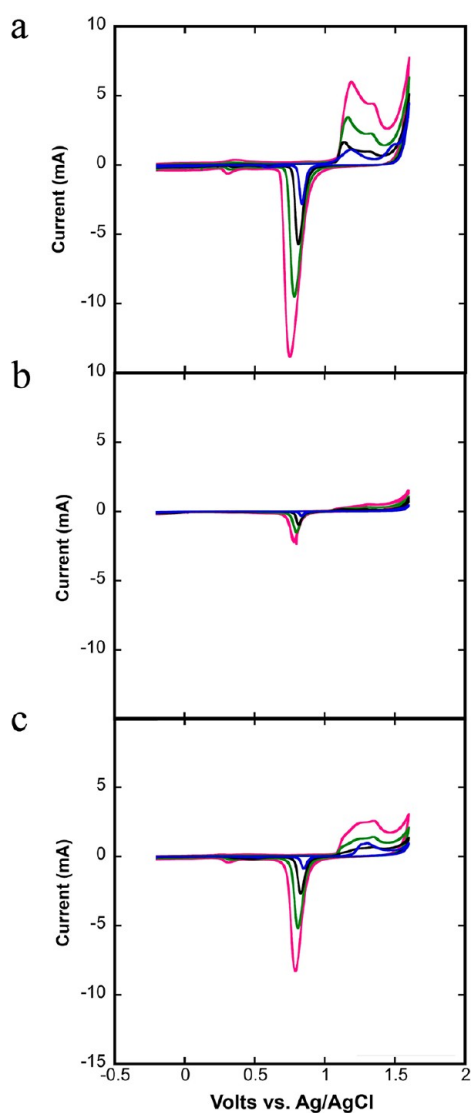
Figure 4. Cyclic voltammograms on (a) porous gold film, (b) solid gold opal, and (c) and porous gold opal electrodes performed in 1 M H₂SO₄ at various scan rates: 100 mV/s (pink), 50 mV/s (green), 20 mV/s (black), and 5 mV/s (blue).

modeled as a vertical line, and this behavior is approximated on the 100 ohm scale. At low impedance scales, we observe circular arc-shaped regions, which are indicative of more complex RC networks. There are no significant regions better described as diffusion-limited redox reactions with a slope of 1, which would indicate a rather vigorous redox process. However, the plots trace arcs at very high impedance values for the alloy electrodes, which could result from a slow, kinetically limited redox process that behaves like a resistance in parallel with the capacitive electrode interface.

At high frequencies, the imaginary component becomes less dependent on frequency, implying an incomplete charge and discharge of the electrodes. The real admittance becomes the larger component. These facts indicate that electrolyte resistance limits current. The highest value seen, at about 100 kHz (above which the instrument bandwidth strongly affects the signal) is about the same in all cases. Here, the electrolyte resistance external to the electrode limits current. Intermediate slopes are signs of the influence of electrolyte resistance within the pores. The intermediate range is small in the case of the
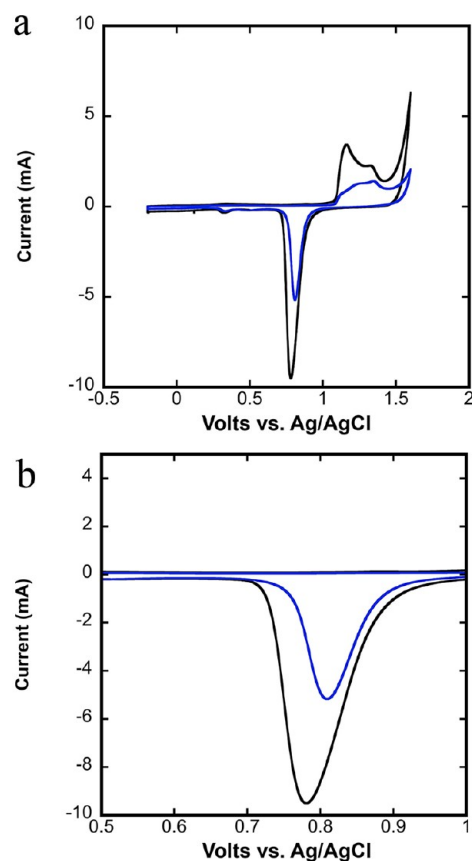

Figure 5. Comparison of (a) cyclic voltammograms collected on a porous gold film (black) and porous gold opal (blue) electrodes in 1 M H₂SO₄ scanned at 50 mV/s. (b) Plot showing a magnified view of the reduction peak from the cyclic voltammograms in (a).
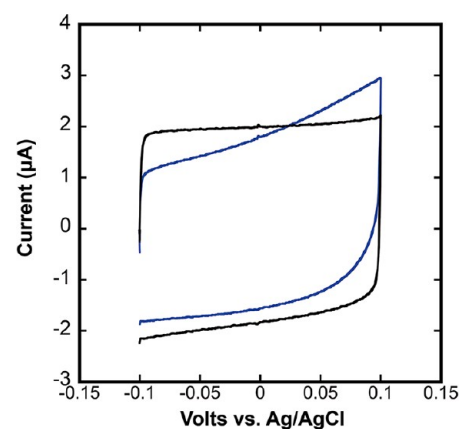

Figure 6. Cyclic voltammograms collected at 10 mV/s comparing the porous gold film (black) and porous gold opal (blue) in 30 mM sodium trifluoroacetate.

solid opal, which shows a relatively sharp transition from capacitive to resistive behavior, but the dealloyed gold samples show a significant intermediate range. Here, the resistance is slightly lower (and therefore admittance is higher) for the porous opal. The spaces between the porous spheres apparently provide wider current paths, and then shorter paths through the narrowest pores.

The admittance data were manually fitted with the de Levie transmission line model, previously developed for comparison to porous gold electrodes.[24] For the dealloyed electrodes, a
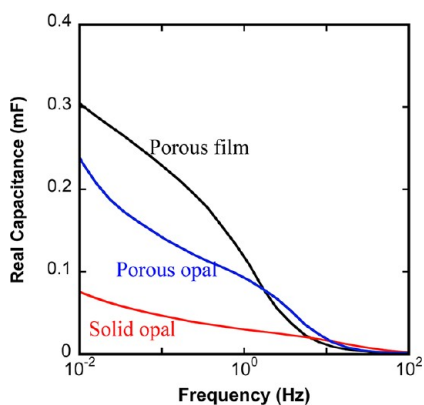
Figure 7. Comparison of real capacitance components as a function of frequency for each electrode.

Figure 9. Schematic of the branched de Levie equivalent circuit model[24,25] used to describe the porous gold opal electrochemical behavior. A resistor in series with both branches represents the solution resistance outside the electrode. The first resistor in the upper branch represents resistance through pores of intermediate size. The other components represent the distributed RC behavior of the interior regions of pores.

branch was included to account for porosity on two length scales, and to improve the fit that was obtained. A schematic of the circuit model is shown in Figure 9. Component values in the fits are presented in Table 1. The capacitances on the lower branch were constrained to be the same, and those on the upper branch were constrained to the surface area ratios versus the solid opal. Dotted lines in Figure 8 illustrate the quality of the fit. (Fits to the impedance and complex capacitance are shown in Figures S2 and S3 of the Supporting Information.) Deviations are greatest at low frequency, where the signals are small, and at high frequency, where the instrument response is significant. Consistent with the qualitative descriptions above, the external resistances are about the same, and the porous film
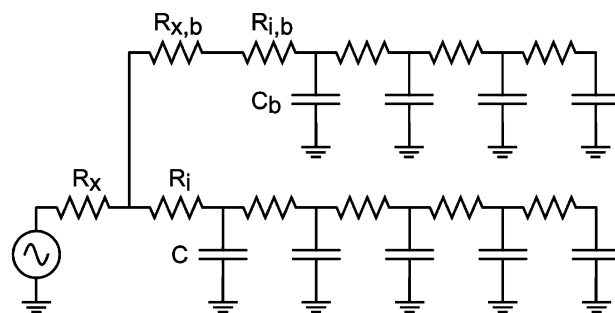
shows both higher capacitance and higher overall resistance versus the porous opal. Because it does not contain designed porosity on an intermediate length scale, one might not expect the porous film to show a strongly double-peaked imaginary component or require a branch for a good fit. Cracks in the film and other nonuniformity in the pore geometry may contribute to this. Resistances contributing to intermediate porosity (internal and branch external) are relatively low for this electrode, suggesting that intermediate porosity is a less significant effect here. The lower-branch internal resistance for the porous opal is quite high, but this parameter is not very significant; its main effect is a shift of the position of the high-
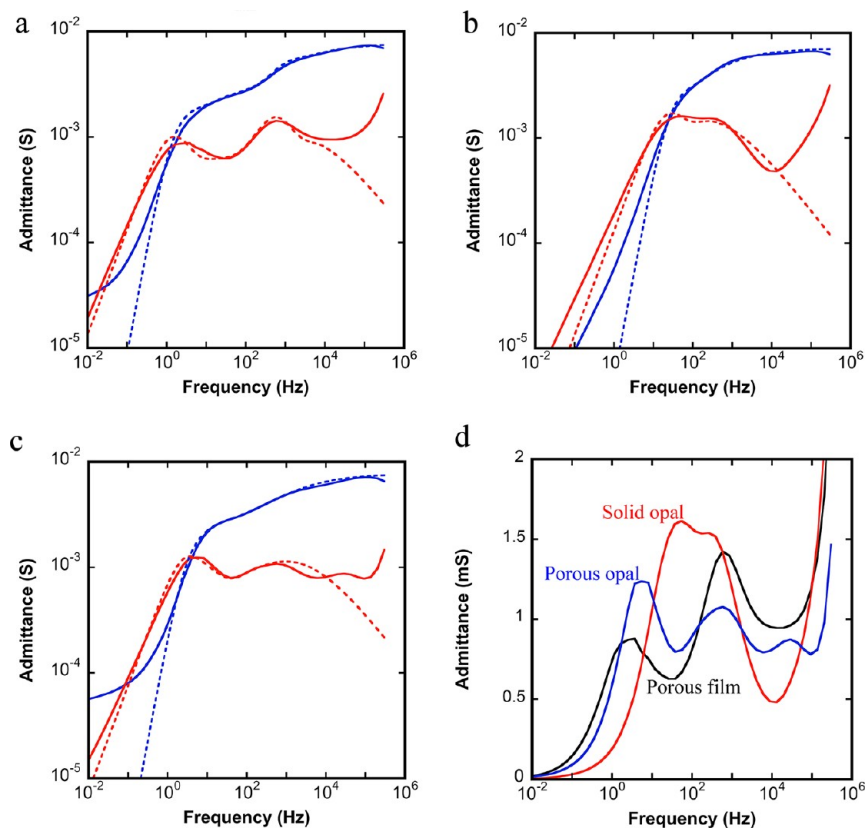

Figure 8. Real (blue) and imaginary (red) admittance components for (a) porous film, (b) solid opal, and (c) porous opal electrodes in 30 mM sodium trifluoroacetate. Dashed lines are fits to the model in Figure 9. (d) Comparison of imaginary admittance components for each electrode.

frequency peak of the imaginary component, which is smaller than the real component.

The most practical significance of these results can be deduced from Figure 8. The real admittance is proportional to the real (dissipated) power, which is a measure of the electrode's inefficiency, whereas the imaginary admittance corresponds to the reactive (stored) power.[26] At frequencies above the lower-frequency peak in the imaginary component, the dissipated power is larger, so the admittance at this peak is a relative measure of the highest practical power that can be delivered from the electrode, and its position is a measure of its fastest operating time scale. The position of the imaginary admittance peak shifts from 2.5 to 55 Hz to 5.5 Hz for the porous film, solid opal, and porous opal, respectively. At slower time scales, more energy can be stored in an electrode with larger capacitance, but at faster time scales, more power can be delivered from an electrode with lower overall internal resistance. Adjusting the different length scales of porosity within an electrode can allow for varying trade-offs between these considerations, with the porous opal offering the possibility for both a large capacitance and low internal resistance.

CONCLUSIONS

We have demonstrated a method to introduce two length scales of porosity in a capacitive porous electrode, a key component of an electrochemical double-layer supercapacitor. One length scale is defined by the naturally formed porosity in a silver–gold alloy when the silver is oxidatively stripped. An inverse opal template forms porosity on the other length scale that is relatively well ordered. Compared to a continuous porous film, the porous gold opal sacrifices some capacitance, but has a lower internal resistance. This means that it can achieve higher power densities, with only a small loss of energy density. To take full advantage of their power density, supercapacitors are best operated on time scales where internal resistance starts to be significant, so there is a need to optimize performance on that time scale.[24] Methods that allow for definition of well-defined, hierarchical porosity, such as those presented here, will allow this. Near these time scales, electrodes with hierarchical porosity can deliver greater amounts of energy than can be achieved with a single porosity scale or a disordered material. For practical use, further work is needed to achieve this level of control on larger scales and with lower-cost materials. Meanwhile, the tractable surface chemistry of gold and the architectural versatility afforded by the ability to template and dealloy it make these approaches a convenient way to gain a quantitative understanding of the effect of an electrode's architecture on its capacity and charging rates. This understanding can guide ongoing efforts to develop electrical energy storage devices tailored to charge and discharge for specific power needs, ranging from microelectronics to regenerative braking to electrical grid storage.

ASSOCIATED CONTENT

Ⓢ Supporting Information

Impedance plots and model fits to the complex capacitance. This material is available free of charge via the Internet at http://pubs.acs.org.

AUTHOR INFORMATION

Corresponding Author

*E-mail: drobins@sandia.gov.

Notes

The authors declare no competing financial interest.

REFERENCES

(1) Kotz, R.; Carlen, M. *Electrochim. Acta* **2000**, *45*, 2483.
(2) Posey, F. A.; Morozumi, T. *J. Electrochem. Soc.* **1966**, *113*, 176.
(3) Bisquert, J. *Phys. Chem. Chem. Phys.* **2000**, *2*, 4185.
(4) Robinson, D. B.; Wu, C. A. M.; Jacobs, B. W. *J. Electrochem. Soc.* **2010**, *157*, A912.
(5) Eikerling, M.; Kornyshev, A. A.; Lust, E. *J. Electrochem. Soc.* **2005**, *152*, E24.
(6) Nilson, R. H.; Griffiths, S. K. *Phys. Rev. E* **2009**, *79*, 036304.
(7) Nilson, R. H.; Griffiths, S. K. *Phys. Rev. E* **2009**, *80*, 016310.
(8) Long, J. W.; Dunn, B.; Rolison, D. R.; White, H. S. *Chem. Rev.* **2004**, *104*, 4463.
(9) Robinson, D. B.; Fares, S. J.; Ong, M. D.; Arslan, I.; Langham, M. E.; Tran, K. L.; Clift, W. M. *Int. J. Hydrogen Energy* **2009**, *34*, 5585.
(10) Biener, J.; Hodge, A. M.; Hayes, J. R.; Volkert, C. A.; Zepeda-Ruiz, L. A.; Hamza, A. V.; Abraham, F. F. *Nano Lett.* **2006**, *6*, 2379.
(11) Erlebacher, J.; Aziz, M. J.; Karma, A.; Dimitrov, N.; Sieradzki, K. *Nature* **2001**, *410*, 450.
(12) Fujita, T.; Qian, L. H.; Inoke, K.; Erlebacher, J.; Chen, M. W. *Appl. Phys. Lett.* **2008**, *92*.
(13) Jin, H. J.; Kurmanaeva, L.; Schmauch, J.; Rosner, H.; Ivanisenko, Y.; Weissmuller, J. *Acta Mater.* **2009**, *57*, 2665.
(14) Senior, N. A.; Newman, R. C. *Nanotechnology* **2006**, *17*, 2311.
(15) Nyce, G. W.; Hayes, J. R.; Hamza, A. V.; Satcher, J. H. *Chem. Mater.* **2007**, *19*, 344.
(16) Trevor, D. J.; Chidsey, C. E. D. *J. Vac. Sci. Technol. B* **1991**, *9*, 964.
(17) Ramirez, P.; Andreu, R.; Cuesta, A.; Calzado, C. J.; Calvente, J. J. *Anal. Chem.* **2007**, *79*, 6473.
(18) Nguyenvanhuong, C.; Clavilier, J.; Bonnemay, M. *J. Electroanal. Chem.* **1975**, *65*, 531.
(19) Chidsey, C. E. D.; Loiacono, D. N. *Langmuir* **1990**, *6*, 682.
(20) Miguez, H.; Meseguer, F.; Lopez, C.; Mifsud, A.; Moya, J. S.; Vazquez, L. *Langmuir* **1997**, *13*, 6009.
(21) Ji, C. X.; Searson, P. C. *J. Phys. Chem. B* **2003**, *107*, 4494.
(22) Campuzano, S.; Pedrero, M.; Montemayor, C.; Fatas, E.; Pingarron, J. M. *J. Electroanal. Chem.* **2006**, *586*, 112.
(23) Trasatti, S.; Petrii, O. A. *Pure Appl. Chem.* **1991**, *63*, 711.
(24) Robinson, D. B.; Wu, C. A. M.; Ong, M. D.; Jacobs, B. W.; Pierson, B. E. *Langmuir* **2010**, *26*, 6797.
(25) de Levie, R. *Electrochim. Acta* **1963**, *8*, 751.
(26) Robinson, D. B. *J Power Sources* **2010**, *195*, 3748.

3979

dx.doi.org/10.1021/am300798j | ACS Appl. Mater. Interfaces 2012, 4, 3973−3979